Sensors and Actuators A 298 (2019) 111586

Contents lists available at ScienceDirect

Sensors and Actuators A: Physical

journal homepage: www.elsevier.com/locate/sna

A silicon optical bench with vertically-oriented micromirrors for active beam steering

Dingkang Wang, Connor Watkins, Sanjeev Koppal, Huikai Xie *

Department of Electrical and Computer Engineering, University of Florida, United States

ARTICLE INFO

Article history:
Received 1 June 2019
Received in revised form 30 August 2019
Accepted 2 September 2019
Available online 3 September 2019

Keywords:
Micromirror
Electrothermal actuation
Bimorph
Forward-view scan
SiOB
LiDAR

ABSTRACT

This paper reports a Silicon Optical Bench (SiOB) integrated with two vertically-oriented tip-tilt micromirrors that can perform active beam steering. The curling of W/SiO_2 bimorphs is utilized to bend microstructures out of plane. The vertical orientation is realized by using a combination of curling W/SiO_2 bimorphs and stoppers. W is employed as one of the bimorph materials to increase the bimorph stiffness, attributed to its much higher Young's modulus than other materials. At the same time, the stress of the W layer is tuned to maximize the bending angle range of the W/SiO_2 bimorphs. The fabrication process of making this new SiOB platform has been developed. Particularly, two electrothermal bimorph-based MEMS mirrors are successfully fabricated and stand upright on an SiOB. The two upright micromirrors are parallel to each other and can perform 2-axis forward-view optical scanning. The mirror plate is made of a 20 μm-thick silicon layer coated with aluminum and its diameter is 0.72 mm. The mirror can rotate $\pm 8^{\circ}$ at 4.5 V. This MEMS scanner has potential applications in miniature LiDAR for Micro Air Vehicles (MAVs).

1. Introduction

Light Detection and Ranging (LiDAR) has attracted enormous attention recently because of its rapidly increasing applications in autonomous vehicles, Unmanned Air Vehicles (UAVs), and ground robotics [1–3]. Motorized optomechanical scanners are the most commonly found type in commercially available LiDAR, but such LiDAR scanners are very energy-inefficient, vulnerable to mechanical shocks and vibrations, and expensive [4]. Thus, reducing their size, weight and power (SWaP) and cost is crucial. Compared to motorized scanners, MEMS scanners are superior in terms of SWaP, scanning speed, and cost [5–7]. Recently many researchers have demonstrated MEMS-based LiDAR [8–11]. For instance, a compact LiDAR system developed by Spectrolab and ARL utilizing an electrostatic MEMS mirror, but this LiDAR still weighed 2.27 kg [8]. However, for most MEMS scanners, the mirror plates of their MEMS mirrors are parallel to the surface of the substrate, so the laser beam must be folded by a fixed mirror to realize forward-view scanning. This requires more components and space as well as extra efforts for precise alignment, making it difficult to further miniaturize LiDAR scanners. It is especially problematic for applying LiDAR on micro-air vehicles (MAVs). MAVs are small drones that can perform various micro-manipulation tasks such as pollinating crops, search and rescue, exploration, and surveillance [12] they typically weigh under 20 g [13]. For instance, the RoboBee developed by Harvard University weighed only 80 mg [10]. So, MAVs require ultra-small LiDAR to detect the surrounding environments, especially the objects in the forward direction.

Thus, in this work, a highly integrated forward-view MEMS LiDAR scanner fabricated directly on a Silicon Optical Bench (SiOB) is proposed. This SiOB based scanner has a pair of vertically-oriented micromirrors and a groove for holding a graded-index (GRIN) lens in the aligned position. In the following, the design, fabrication process and device characterization are sequentially described.

2. Device design

As illustrated in Fig. 1, the proposed LiDAR scanner consists of two vertically-oriented 2-axis micromirrors, an alignment trench, and a GRIN lens, all integrated on a silicon substrate. As can be seen in this figure, the two MEMS mirrors are lifted up at 90° by a bending mechanism, and the vertical orientation is secured by a stopper. The 2-axis scanning MEMS mirror design is similar to the one reported in [14]. The innovation of this work lies in the implementation of forward-view scanning with two vertical mirrors as well as how to

* Corresponding author.
E-mail addresses: noplaxochia@ufl.edu (D. Wang), watkins.connor@ufl.edu (C. Watkins), hkxie@ece.ufl.edu (H. Xie).

https://doi.org/10.1016/j.sna.2019.111586
0924-4247/

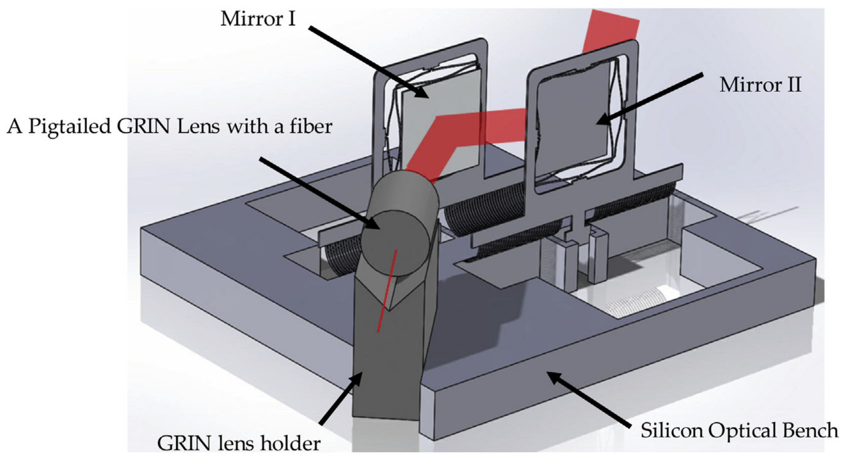

Fig. 1. The proposed optical forward-view scanner integrated on an SiOB.

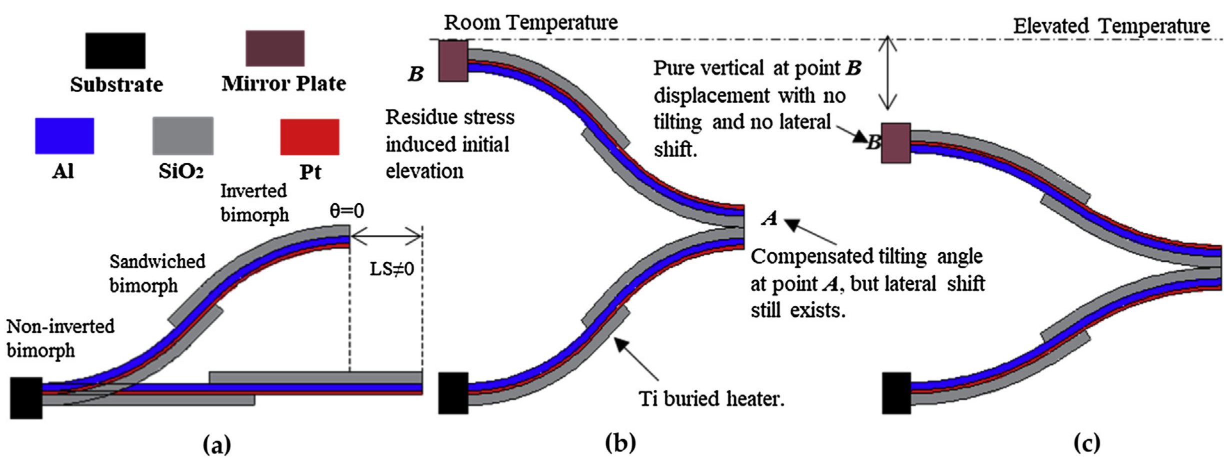

Fig. 2. The principle of the Al/SiO_2 ISC bimorph actuator: (a) One inverse series connected (ISC) bimorph, θ = 0, LS ≠ 0. (b) Folded ISC, θ = 0, LS = 0. (c) Pure vertical displacement with temperature change.

realize the vertical bending mechanism with high stiffness and the stoppers for vertical positioning.

2.1. *Design of the electrothermal 2-axis scanning mirrors*

The 2-axis micromirrors are electrothermally actuated, based on the inverted-series-connected (ISC) bimorph actuation structure reported in [15]. A single ISC bimorph actuator design is shown in Fig. 2(a), which consists of three segments: an inverted bimorph, a sandwiched overlap, and a non-inverted bimorph. The single ISC structure leads to zero tangential tip angle θ but with some lateral shift (LS) during actuation. By connecting two ISC actuators in a folded fashion, both θ and LS are compensated, as shown in Fig. 2(b) and (c). In this work, SiO_2 and Al are used as the two bimorph materials while Pt is used as the embedded heater material (not shown).

The topology design of the electrothermal MEMS mirror is shown in Fig. 3, where a central mirror plate is suspended by four ISC actuators. Increasing the size of the mirror plate will decrease the scan angle and scan speed, so the size of the mirror plate should be minimized. On the other side, the mirror plate size (diameter or side length, d) determines the divergence angle, θ, of the scanned laser beam (wavelength, λ_0), i.e., $\theta \cong \frac{2\lambda_0}{\pi d}$. To achieve a 1-cm resolution at 3 m distance, a scanned laser beam diameter of 0.52 mm or larger is needed. The size of the mirror plate should be larger than the laser beam size to reflect most of the laser power with minimal loss. In this design, a square mirror with an edge length of 0.72 mm is chosen to balance the scanning angle and the angular resolution.

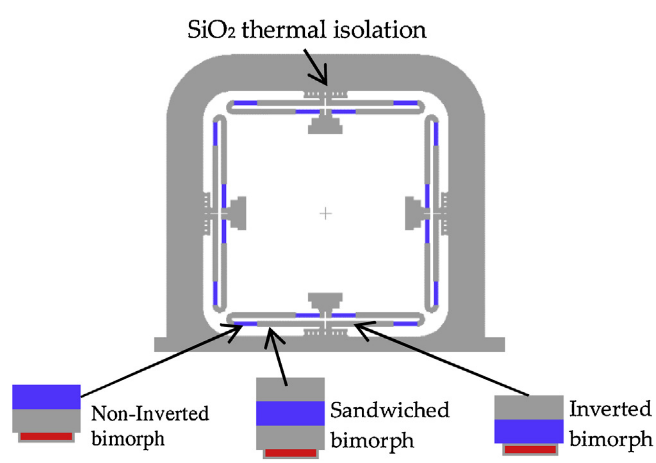

Fig. 3. Device topology with the detailed bimorph layer.

COMSOL is used for simulation of the mirror and the result is seen in Fig. 4. According to the static response simulation, the maximum displacement of the bimorph actuator is expected to be 60 μm if heated to 300 °C, which leads to a mechanical tip-tilt angle of 4.5° in each direction, shown in Fig. 4(a). Also, according to the modal simulation shown in Fig. 4(b), the resonant frequency of the tip-

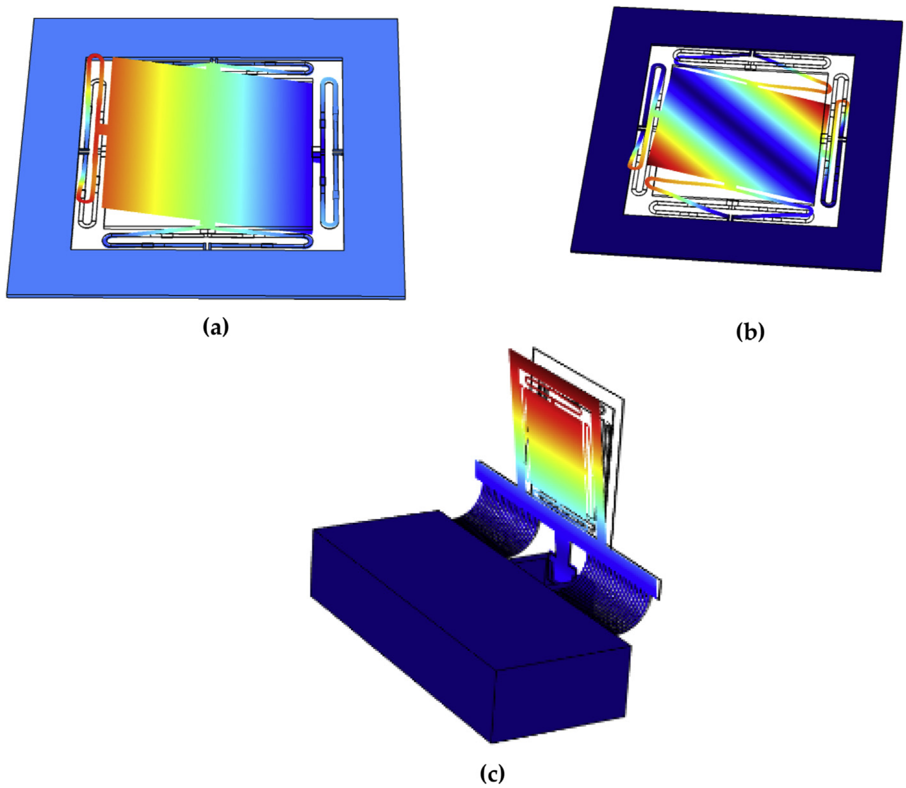

Fig. 4. (a) The COMSOL simulation result of the static response shows a mechanical scanning range of ±4.5° at 300 °C. (b) Simulation of the frequency response shows the tip-tilt scanning mode is at 1.5 kHz. (c) The frame rotation mode with the curved bimorphs is at 890 Hz.

tilt mode is 1.5 kHz, assuming a 20 μm thick single-crystal-silicon mirror plate is used. This thick mirror plate is employed to ensure mirror rigidity and flatness.

2.2. Design of the vertical bending mechanism with high stiffness bending bimorph array

The SiOB requires vertical orientation of the micromirrors. The fabrication process design is challenging in how to release such complex, out-of-plane microstructures properly. Surface-micromachined micro-hinge technology was used to fabricate out-of-plane micro-optical components [16,17], but in this process, the mirror plate needs to be pulled up manually to the vertical position, and it is difficult to deliver electrical signals to the actuators through the hinge. Thus, an alternative vertical orientation mechanism on a SiOB is needed. Previously, 45° and 90° tilted MEMS mirrors were developed for endomicroscopic imaging and Fourier transform spectrometers [14,18], in which the bending cantilever arrays utilized the residual stresses in Al/SiO_2 bimorphs, but Al thin films typically do not have high residual stresses (~100 MPa), which means long Al/SiO_2 bimorphs are needed to bend large angles. Meanwhile, both Al and SiO_2 only have modest Young's moduli (~ 70 GPa). Therefore, the bending bimorph arrays suffer from low stiffness and thus may be easily broken. So, higher stiffness is needed to ensure a robust design.

Tungsten (W) is a commonly used semiconductor material with a high Young's modulus (411 GPa), and replacing Al with W will significantly improve the stiffness. Another reason for using W is its high residual stress. Fig. 5 shows the relationship between the W residual stress and the Ar pressure, where the W film was deposited by a KJL CMS-18 sputter system. As can be seen in Fig. 5, the residual stress of W films can be tuned from -1.5 to 2.5 GPa, and the data points can be approprimately fitted with a 3[rd] order polynomial curve. To bend bimorph beams, the residual stresses should be tensile on one side and compressive on the other side. Since the residual stress of PECVD SiO_2 is compressive at about 500 MPa, the residual stress of W is set at about 1.5 GPa tensile stress. Then the Ar pressure should be about 6.2 mT in the sputter system. Higher stresses were not chosen because W was peeling-off when W had tensile stresses above 2 GPa.

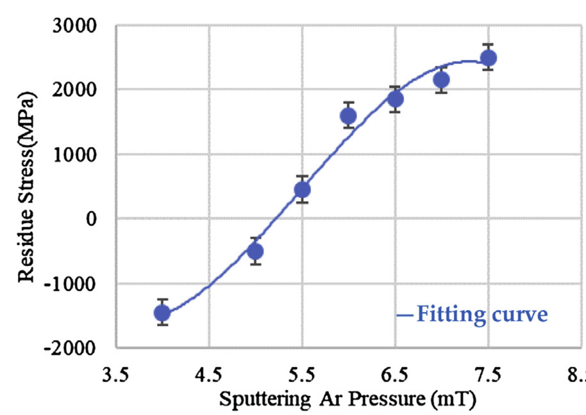

Fig. 5. The relationship between the Ar pressure of W sputtering and the tungsten residual stress.

The width of a single W/SiO_2 bimorph (w) is limited to 21 μm and the gap between W/SiO_2 bimorphs is 30 μm for the consideration of the release process. More bimorphs can contribute to higher combined stiffness, but the dimension of the SiOB limits the total number of bending bimorphs. The stiffness of a single bimorph (k) is a function of the thicknesses of W (t_W) and SiO_2(t_{ox}), and the

Table 1
Design parameter values.

Fixed Variables	
***w* = 21 μm**	// width of a single bimorph
σ_{ox} = -0.5 GPa	// residual stress of the PECVD SiO_2
σ_W = 1.5 GPa	// residual stress of the sputtered W
E'_{ox} = 84.3 GPa	// biaxial Young's modulus of SiO_2
E'_W = 562 GPa	// biaxial Young's modulus of W
Optimization results	
***L*= 350 μm**	//length of one bending bimorph
t_{ox}= 1 μm	//thickness of the SiO_2 layer
t_{ox}=0.39 μm	//thickness of the W layer
***EI* =4.1×10−12 N·m2**	// stiffness of one bending bimorph
***k* = 0.29 N/m**	// stiffness of one bending bimorph

length of the bimorph (L). The constraint is that the bending angle θ should be greater than 90°. The bending angle is given by [19]:

$$\theta = \frac{Lm_A}{EI}\left(\frac{\sigma_W}{E_W'} - \frac{\sigma_{ox}}{E_{ox}'}\right) \geq 90^\circ \quad (1)$$

Here the moment of inertia of the bending bimorph, m_A, is given by

$$m_A = \frac{w\,(t_W + t_{ox})\,t_W t_{ox} E_W' E_{ox}'}{2\left(t_W E_W' + t_{ox} E_{ox}'\right)} \quad (2)$$

and EI is given by:

$$EI = \frac{w}{12}\frac{t_W^4 E'^2_W + t_{ox}^4 E'^2_{ox} + t_W t_{ox} E'_W E'_{ox}\left(4t_W^2 + 4t_{ox}^2 + 6t_W t_{ox}\right)}{t_W E'_W + t_{ox} E'_W} \quad (3)$$

The stiffness of a single bimorph (k) is given by:

$$k = \frac{3EI}{L^3} \quad (4)$$

Intuatively, thicker SiO_2 and W layers are preferred for large k, but thicker layers increase m_A (Eq. (2)), and consequently requires a longer bimorph length L to meet the $\Theta \geq 90^\circ$ constraint (Eq. (1)), which unfortunately will decrease k (Eq. (4)). The analytical solution to this problem is quite complex, so a numerical optimization is performed using the Optimization Toolbox in MATLAB [20].

For the optimization, Eqs. (1)–(4) are input to the Optimization Toolbox to maximize k, where $\boldsymbol{t_{ox}}$, $\boldsymbol{t_W}$, and L are the variables, $\theta \geq 90^\circ$ as the contraints, and the corresponding parameter values are listed in Table 1. The output of the toolbox is not a single solution. There are multiple sets of $\boldsymbol{t_{ox}}$, $\boldsymbol{t_W}$ and L values all corresponding to the maximum k, which is 0.29 N/m. After analyzing all the data sets, we have found the following relationships among the three variables for the maximum k:

$$\frac{t_{ox}}{t_W} = \sqrt{\frac{E_W'}{E_{ox}'}} = 2.58 \quad (5)$$

$$\frac{L}{t_{ox}} \approx 350 \quad (6)$$

Since the maximum stiffness k is always 0.29 N/m with every optimized combination of the layer thicknesses and the bimorph length, the actual layer thicknesses and the bimorph length can be chosen according to Eqs. (5) and (6). With the practical deposition process considered, the thicknesses of W and SiO_2 are selected as 0.39 μm and 1.0 μm, respectively. As a result, the bimorph length needed for 90° bending is 350 μm. To guarantee at least 90° bending with process variations considered, the actual length in the layout design is set as 400 μm. With these structure parameters, the total stiffness of the forty-eight bending bimorph array is calculated as 13.9 N/m, which corresponds to a frame rotational resonant mode of 1.2 kHz. The total stiffness is 56 times greater comparing to the previous Al/SiO_2 bimorph array [14], this will improve the resistance to vibration.

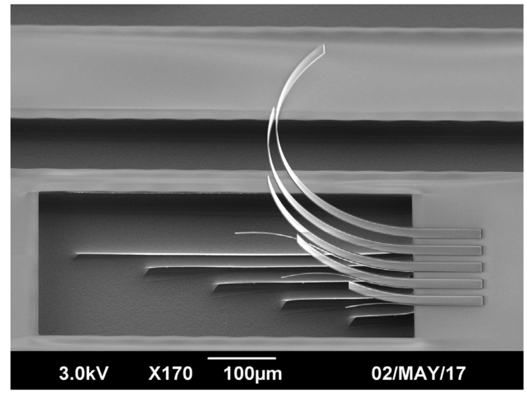

Fig. 6. An SEM of the W/SiO_2 bimorph test structures with different lengths.

Table 2
The tip bending angles of the test bimorph structures.

Length of test bimorph structures	100 μm	200 μm	300 μm	400 μm	500 μm
Theoretical tip bending angle	26°	51°	77°	103°	129°
Measured tip bending angle	27°	54°	79°	102°	131°

A test structure with the designed W and SiO_2 thicknesses has been fabricated using the W process described above. As shown in Fig. 6, all of the five test bimorph structures have a similar curvature, which are approximately 1.5× greater than the Al/SiO_2 bimorphs [14]. The bending angles of the test structures are listed in Table 2. Note that it is difficult to measure the tip angles of the bending structures accurately. The errors of the measured values in Table 2 are about ±3°. Thus, 400 μm-long W/SiO_2 bimorphs meet the need for vertical orientation. The W layer of the bending bimorph is also used to conduct electrical current to the bimorph actuators of the two MEMS mirrors.

2.3. The stopper structure and the optical geometrical design

The bending bimorph array is intentionally designed longer so that the mirror frame will be bent at least 90° even with the process variations considered. Thus, in order to achieve exactly 90° vertical bending, a stopper is designed on the SiOB. The stopper is illustrated in Fig. 7. As can be seen, the mirror frame has a T-shaped bar extruded. The T bar is made with the silicon of the device layer, so it is rigid. Meanwhile, a silicon wall is formed on the silicon substrate so that the T bar of the mirror frame is precisely stopped by the silicon sidewall when the bimorphs are released.

The optical design of the scanner is shown in Fig. 8, where two MEMS mirrors stand vertically on the SiOB and are parallel to each other. Note that the first MEMS mirror is mainly used as a stationary mirror to fold the laser beam. The first mirror can also be actuated for two-axis tilting to compensate for the misalignment. The misalignment may come from the mirror frames, the released mirror plates or the GRIN lens holder. A 0.5 mm-diameter GRIN lens is chosen to collimate the laser beam to about 0.35 mm in diameter. The laser beam is incident on the first MEMS mirror and then bounces off the second MEMS mirror both at 45°. The laser spot on the second MEMS mirror plate becomes 0.5 mm due to the 45° incident angle. When the second MEMS mirror tilts 5°, the laser spot on the second mirror plate is increased to 0.54 mm. The mirror plate is designed as 0.7 mm × 0.7 mm so that the entire laser beam is reflected. The distance between the two mirrors is set to 1.3 mm to ensure that the laser spot reaches both mirrors with-

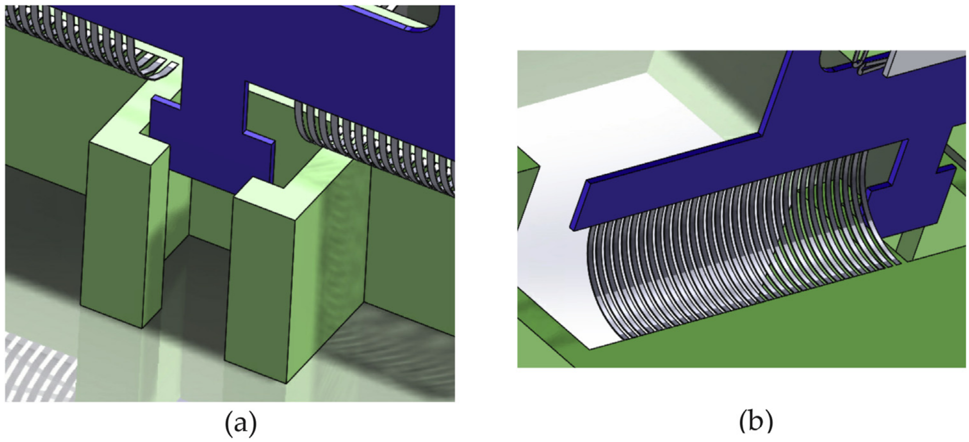

Fig. 7. (a) The stopper structure design. (b) W/SiO_2 bending bimorph array.

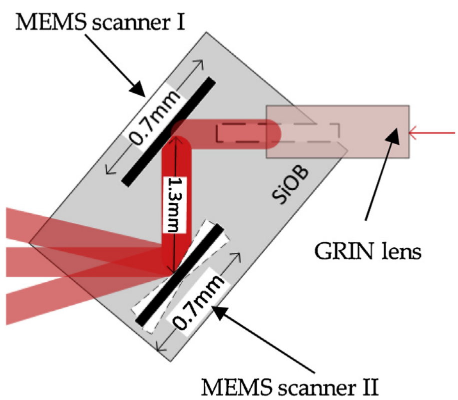

Fig. 8. Optical design of the proposed integrated optical scanner.

out being truncated. If both mirrors actively scan, then the mirror distance and mirror size must be carefully designed to avoid laser beam truncation. The weight of the entire MEMS scanner is just 16 mg, which can even be carried by a RoboBee [13].

3. Device fabrication

The fabrication process flow is illustrated in Fig. 9. The process is done on an SOI wafer with a device layer of 20 μm, a 1 μm-thick buried oxide (BOX) layer and a 500 μm-thick handle layer. First, a 1-μm-thick PECVD SiO_2 layer is deposited and wet-etched on the front side of the SOI wafer to form the bottom layer for the bimorphs containing SiO_2 as the bottom layer. Then a Cr/Pt/Cr lift-off process is performed to form the heaters for the bimorph actuators, followed by sputtering a 0.39-μm-thick W layer with high tensile stress and performing a lift-off of the W layer for the vertical bending bimorph array. The Ar pressure during W sputtering is set at 6.2 m T. After that, a 0.1-μm-PECVD SiO_2 layer is deposited and patterned using RIE, and then a 0.9 μm Al layer is sputtered and patterned by a lift-off process to form the other layer of the bimorph actuators as well as the electrical wiring, pads and mirror surface coating. Another 1.2-μm-PECVD SiO_2 layer is deposited and patterned by RIE dry etch to form bimorph actuators with SiO_2 as the top layer. A silicon carrier wafer is attached to the front side of the SOI wafer for DRIE etch with a 200-nm sputtering Al_2O_3 as the mask. The DRIE etch stops at the BOX layer. Then the BOX layer is removed through RIE. After this step, the device wafer is separated from the carrier.

The release starts with an anisotropic DRIE that etches through the device layer to expose the sidewalls of the silicon underneath the bimorphs. Then an isotropic etch is done to undercut the silicon blocks to release the bimorphs including both the bimorph actuators and the vertical bending bimorph array. Residual stresses in the thin films of the bimorphs result in initial out-of-plane displacement.

The final release only takes one step but needs careful design and precise DRIE timing control. The bimorph actuators must be released before the release of the vertical bending bimorphs. Otherwise the silicon on the backsides of the mirror plate and the mirror frame will be quickly etched when the mirror frame is tilted up. The release is achieved by designing the width of the actuator bimorphs smaller than that of the vertical bending bimorphs. In this way, the silicon beneath the actuator bimorphs will be etched completely when the silicon underneath the vertical bending bimorphs is still only etched partially. Thus, the actuator bimorphs are released before the vertical bending bimorphs starts to curl. Continuing the isotropic etching releases the vertical bending beams that bring the two micromirrors to rotate out of plane. Meanwhile the stoppers on the frames of the two micromirrors stop the frames at their vertical standing positions.

Fig. 10(a) shows an SEM of a fabricated device, where the two vertically-oriented micromirrors are each driven by four ISC electrothermal Al/SiO_2 bimorph actuators [14], and the groove for the GRIN lens is 45° to the mirrors. As can be seen from the SEM of one vertical micromirror in Fig. 10(b), the initial elevation of the mirror plate is about 155 μm and the mirror plate is parallel to the mirror frame. The actuators form dual-S-shaped structures because of the residual stress. Details of the bent W/SiO_2 bimorph array and the stoppers are shown in the SEMs in Fig. 10(c) and (d).

4. Device characterization

4.1. Scanning characterization

The measured static scan response and frequency response are plotted in Fig. 11(a) and Fig. 11(b), where an optical scan range of ±8.5° is obtained at a maximum voltage of 4.5 Vdc for both axes. The maximum power consumption of each actuator is 40 mW, the linear scan range is from 1° to 8° and the tip-tilt angular scan mode is at 2.2 kHz, which is greater than the designed 1.5 kHz. This increased resonance frequency is attributed to the mirror plate thinned down by the last DRIE release step. A step response measurement shows that the measured rise time is 2.4 ms, as shown in Fig. 11. (c). The forward scanning patterns generated by the MEMS mirrors are shown in Fig. 12. Fig. 12(a) is a resonant line scanning pattern with a driving signal of f =2.2 kHz and Vpp = 4 V applied to one of the bimorph actuators. Note that the pattern is not a straight line but

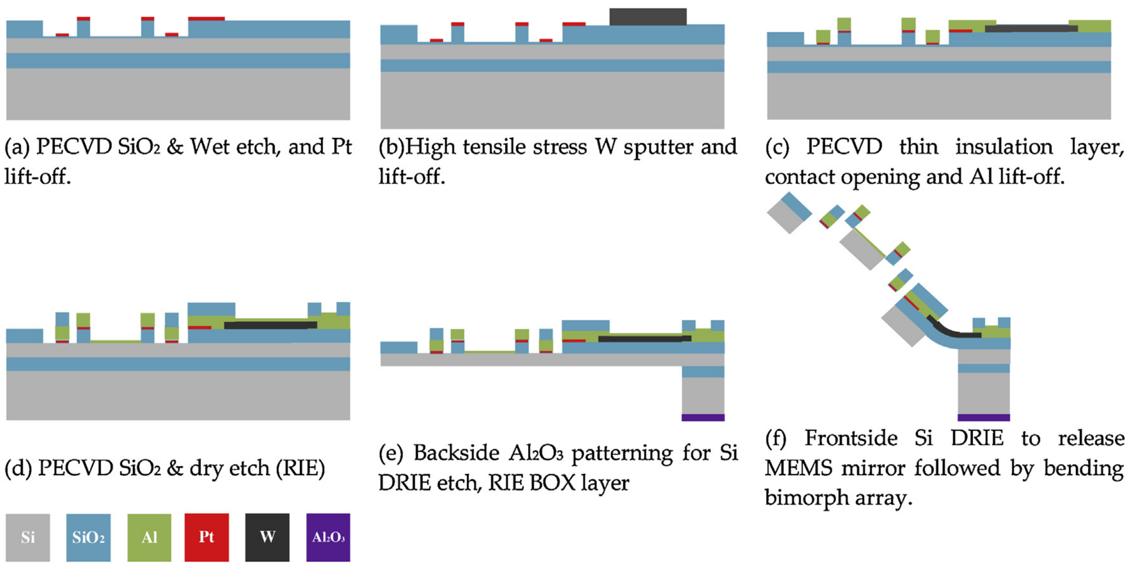

Fig. 9. The fabrication process flow.

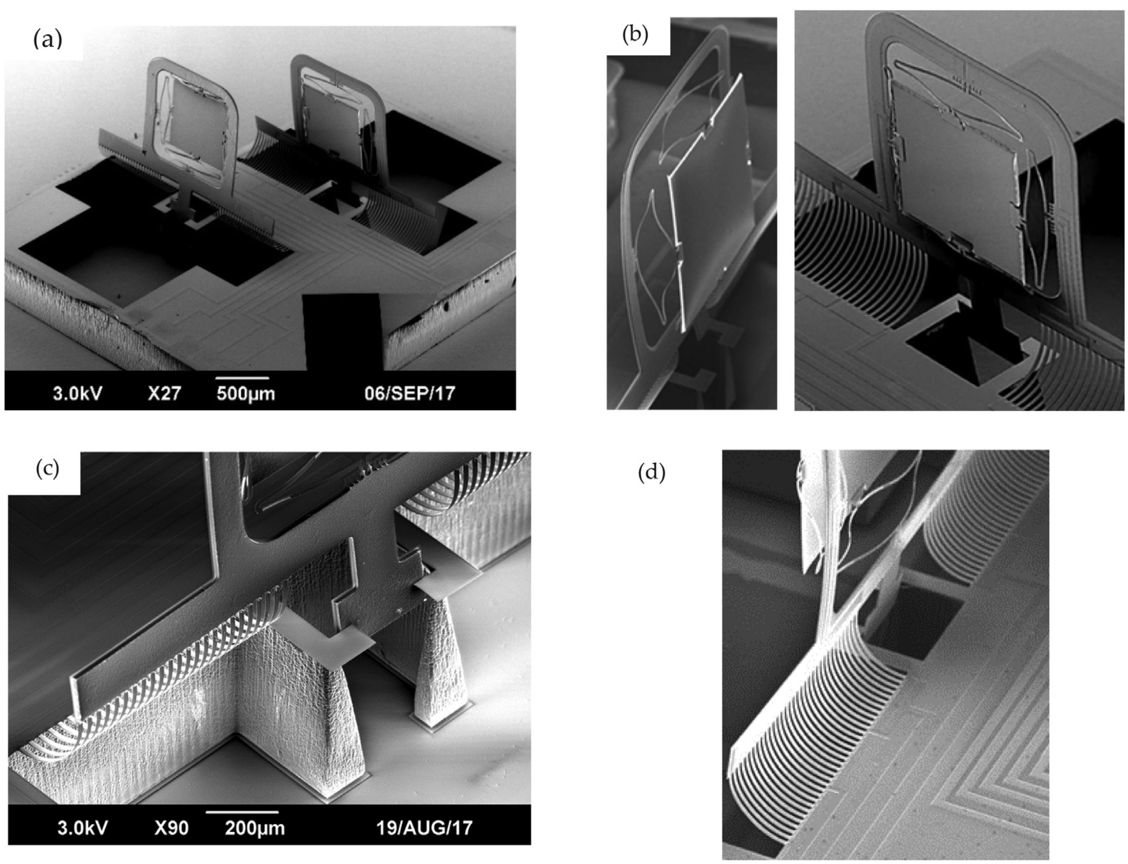

Fig. 10. (a) An SEM of the fabricated MEMS scanner. (b) SEMs of one MEMS mirror with Al/SiO_2 bimorph actuators. (c) An SEM of the stopper. (d) An SEM of the W/SiO_2 bending bimorph array.

a long, narrow ellipse instead. This is due to the symmetry of the mirror design, leading to degenerate x- and y- rotational modes. Thereby, the y rotational mode will be excited when the mirror is driven to resonance at x rotation. The line scanning angle is 30°, and the cross-axis coupling angle is only 1.5°. Fig. 12(b) is a non-resonant raster scanning pattern over a FoV of 7° by 4°. The slow axis is driven at f =7 Hz, Vpp = 4 V, and the fast axis is driven at f =320 Hz, Vpp = 4 V.

4.2. Bending bimorph array characterizations

The measured first resonant mode occurred at 1.03 kHz, as shown in Fig. 11(b), which was identified as the frame rotation mode. The stiffness of the bimorph array was more than 20 times greater than that of the Al/SiO_2 bending bimorph array reported in a previous work [14] because the Young's modulus of W is much higher than that of Al, making the W based bending bimorph array

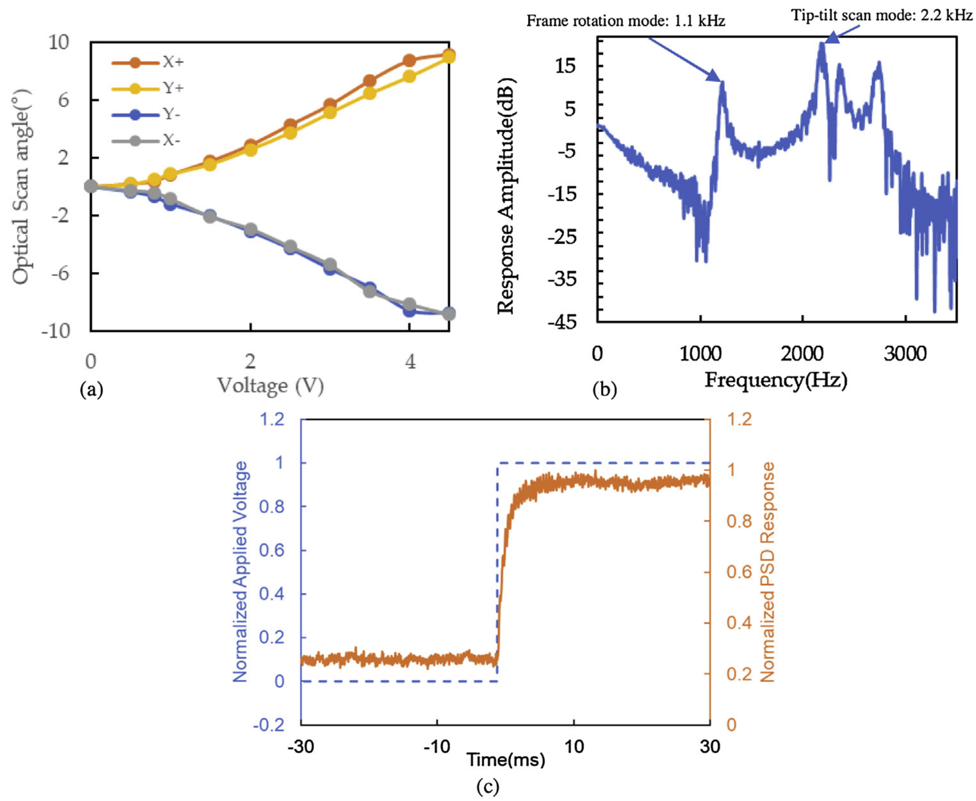

Fig. 11. Static response (a), frequency response (b) and step response (c) of the MEMS scanner.

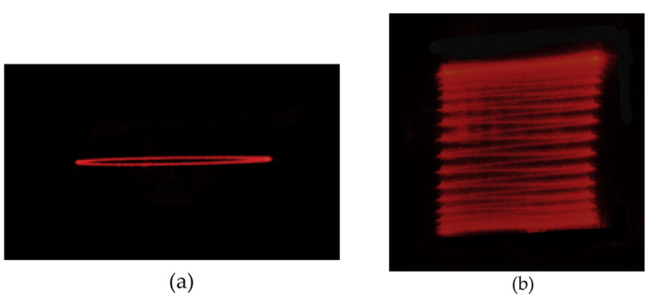

Fig. 12. (a) A resonant line scan pattern with 30°scanning angle at 2.2 kHz. (b) A raster scan pattern generated by driving the fast axis at 320 Hz and the slow axis at 7 Hz.

much more robust. All of the mirror frames were bent upright automatically after the final release step. Due to the process variations, the upright orientation angles of the mirror frames on different scanners were different. The measured bending angles ranged from 85° to 97°. Fortunately the bending angle variations could be compensated through driving the first micromirror to direct the laser beam precisely to the second micromirror. The main issue was that the silicon substrate of the stopper structure was over-etched in some cases during the release step, as shown in Fig. 10(c), causing the silicon wall to be partially broken and the bending angle to exceed the designed position. This issue can be mitigated via better dimensional design and release process optimization.

The bending bimorph array also conducts electrical current to the bimorph actuators of the MEMS mirrors. Although the resistance of the conducting layer on the bending bimorphs is small, there is still some Joule heating generated on the bending bimorphs. Thus, the mirror frames will bend slightly when actuating the central mirror plates. To measure the drift of the mirror frame under continuous operation over time, an experiment was designed to accelerate the aging of the bending bimorph array. A MEMS mirror frame was continuously driven at the frame rotational resonant frequency of 1.03 kHz with Vpp = 4 V. At this resonant frequency, the mirror frame vibrated by 1.5°, which is much greater than the bending angle under normal operation. The result is plotted in Fig. 13(a), showing that the angular drift of the mirror plate was only 1° after approximately 700 h or 1 billion cycles of large bending.

The temperature drift of the mirror plate orientation was also tested. The result is shown in Fig. 13(b). As can be seen, when the ambient temperature varied from 25 °C to 80 °C, the mirror frame rotated only about 1°, which typically is negligible. This small orientation angle change is attributed to the small thermal expansion coefficient difference between W and SiO_2. The temperature drift and temporal drift can also be easily compensated by driving the first MEMS micromirror when the ambient temperature changes.

4.3. Disccusion

As can be seen from Fig. 10(c), the mirror frame is stopped only on one side, so the mirror frame still has a tenency to move back when there is an external acceleration or a shock. A latching mechanism will be developed in the future. According to the test results presented in Section 4.1, both upright MEMS mirrors are capable of quasi-static scan of up to 17 °FOV and resonant scan of up to 30 °FOV. As shown in Fig. 1, the two upright micromirrors are parallel to each other. There are three major operation modes: 1) both mirrors scan 2 axes with one axis at resonance and the other at linear scan; 2) both mirrors scan 2 axes with both axes at linear scan; and 3) Mirror 1 does not scan while Mirror 2 provides the 2-axis scanning.

For operation mode 1, the pair of MEMS mirrors can generate a raster scan with a large FOV of 60°×34°. Compared to resonant scans of electrostatic micromirrors [20], the resonance of these electrothermal micromirrors have a much lower quality factor (50

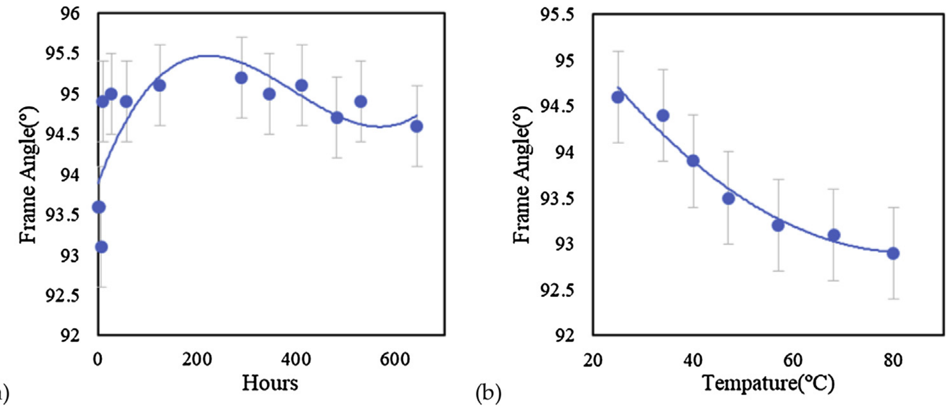

Fig. 13. Temporal drift (a) and thermal drift (b) of the rotation of the mirror plate.

versus over 49,300), so the phase stability is improved. One issue of operation mode 1 is that the resonant frequencies of the two micromirrors may be different due to process variations, requiring precise phase tuning. Also, the optical beam reflected by Mirror 1 may be truncated by Mirror 2, leading to power loss and large beam divergence. For operation mode 2, the pair of MEMS mirrors can generate a raster scan with a FOV of $34^{\circ}\times34^{\circ}$ or any programmable arbitrary scan patterns within that FOV. This operation mode overcomes the phase issues, but the beam truncation still remains. For operation mode 3, it can generate a raster scan with a FOV of $17^{\circ}\times17^{\circ}$ or any programmable arbitrary scan patterns within that FOV. The FOV in mode 3 is smaller than those of operation modes 1 and 2, but there are no beam truncation issues. Meanwhile, Mirror 1 is not only used to fold the incident optical beam for forward scanning, but can also be used to compensate any optical misalignments caused by microfabrication or the assembly process.

The main advantage of this optical scanner design is that it provides forward-view scanning at small size. The all-in-one forward scanning MEMS scanner eliminates the fixed mirror and the alignment holder needed for other MEMS scanners for LiDAR [2,3,11]. The entire forward-view scanner (with a GRIN lens included) has a form factor of only 4 mm × 4.5 mm × 1.6 mm and weighs just 16 mg. Thus, this scanner has potential applications in MAVs as well as in optical endoscopic imaging.

5. Conclusions

In this work, a novel Silicon Optical Bench (SiOB) platform with active beam steering/scanning is proposed and experimentally verified. The vertical standing of micromirrors on the SiOB is achieved by using high-stiffness W/SiO_2 bimorphs and on-chip stoppers. A miniature LiDAR based on this MEMS scanner is being built and the development of a new latching mechasim that can further secure the upright mirrors is ongoing. This robust SiOB platform allows monolithic integration of multifunctional optical components and easy optical alignment. Vertically-oriented MEMS mirrors integrated on the SiOB can form ultra-compact forward-viewing optical scanners. This compact forward-view scanner is ideal for MAVs and has a great potential for applications in insect-sized MAVs. It also has other potential applications such as endoscopic optical imaging and Michelson interferometers.

Acknowledgements

This work is supported by the National Science Foundation, USA under the award #1514154, the Office of Naval Research, USA under the award #N00014-18-1-2663 and the US NSF I/UCRC program - MIST Center.

References

[1] C. Niclass, K. Ito, M. Soga, H. Matsubara, I. Aoyagi, S. Kato, M. Kagami, Design and characterization of a 256x64-pixel single-photon imager in CMOS for a MEMS-based laser scanning time-of-flight sensor, Opt. Express 20 (11) (2012) 11863–11881, http://dx.doi.org/10.1364/OE.20.011863.
[2] D. Wang, S. Strassle, A. Stainsby, Y. Bai, S. Koppal, H. Xie, A compact 3D lidar based on an electrothermal two-axis MEMS scanner for small UAV Laser Radar Technology and Applications XXIII, Vol. 10636, International Society for Optics and Photonics, 2018, p. 106360G.
[3] B.L. Stann, J.F. Dammann, M.M. Giza, Progress on MEMS-scanned ladar Laser Radar Technology and Applications XXI, Vol. 9832, International Society for Optics and Photonics, 2016, p. 98320L.
[4] Optical Encoders and LiDAR Scanning, 2018, Available online: http://www.renishaw.com/en/optical-encoders-and-lidar-scanning–39244 (Accessed on 24th November 2018).
[5] U. Hofmann, J. Janes, MEMS Mirror for Low Cost Laser Scanners. Advanced Microsystems for Automotive Applications, Springer, Berlin, Heidelberg, 2011, 2011; pp. 159-165, 978-3-642-21380-9.
[6] S.T. Holmstrom, U. Baran, H. Urey, MEMS laser scanners: a review, JMEMS 23 (2) (2014) 259–275, http://dx.doi.org/10.1109/JMEMS.2013.2295470.
[7] D. Wang, X. Zhang, L. Zhou, M. Liang, D. Zhang, H. Xie, An ultra-fast electrothermal micromirror with bimorph actuators made of copper/tungsten, Optical MEMS and Nanophotonics (OMN), 2017 International Conference (2017) 1–2.
[8] R. Moss, P. Yuan, X. Bai, E. Quesada, R. Sudharsanan, B.L. Stann, W.B. Lawler, Low-cost compact MEMS scanning ladar system for robotic applications Laser Radar Technology and Applications XVII, Vol. 8379, International Society for Optics and Photonics, 2012, p. 837903.
[9] Katsumi Kimoto, et al., Development of small size 3D LIDAR, in: 2014 IEEE International Conference on Robotics and Automation (ICRA), IEEE, 2014.
[10] K. Ito, C. Niclass, I. Aoyagi, H. Matsubara, M. Soga, S. Kato, et al., System design and performance characterization of a MEMS-based laser scanning time-of-flight sensor based on a 256×64-pixel single-photon imager, IEEE Photonics J. 5 (2) (2013) 6800114.
[11] A. Kasturi, V. Milanovic, B.H. Atwood, J. Yang, UAV-borne lidar with MEMS mirror-based scanning capability Laser Radar Technology and Applications XXI, Vol. 9832, International Society for Optics and Photonics, 2016, p. 98320M.
[12] K. Dantu, S. Berman, B. Kate, R. Nagpal, A comparison of deterministic and stochastic approaches for allocating spatially dependent tasks in micro-aerial vehicle collectives, in: 2012 IEEE/RSJ International Conference on Intelligent Robots and Systems, IEEE, 2012, pp. 793–800.
[13] D. Floreano, R.J. Wood, Science, technology and the future of small autonomous drones, Nature 521 (7553) (2015) 460, http://dx.doi.org/10.1038/nature14542.
[14] C. Duan, W. Wang, X. Zhang, L. Zhou, A. Pozzi, H. Xie, A self-aligned 45°-tilted two-axis scanning micromirror for side-view imaging, JMEMS 25 (4) (2016) 799–811, http://dx.doi.org/10.1109/JMEMS.2016.2562011.
[15] K. Jia, S. Pal, H. Xie, An electrothermal tip–tilt–piston micromirror based on folded dual S-shaped bimorphs, JMEMS 18 (5) (2009) 1004–1015, http://dx.doi.org/10.1109/JMEMS.2009.2023838.
[16] M.C. Wu, L.Y. Lin, S.S. Lee, K.S.J. Pister, Micromachined free-space integrated micro-optics, Sens. Actuators A: Phys. 50 (1-2) (1995) 127–134, http://dx.doi.org/10.1016/0924-4247(96)80096-3.
[17] L.Y. Lin, S.S. Lee, K.S.J. Pister, M.C. Wu, Three-dimensional micro-Fresnel optical elements fabricated by micromachining technique, Electron. Lett 30 (5) (1994) 448–449, http://dx.doi.org/10.1049/el:19940277.
[18] W. Wang, J. Chen, Q.A. Tanguy, H. Xie, A monolithic michelson interferometer with a large piston MEMS micromirror, in: Optical MEMS and Nanophotonics (OMN), 2016 International Conference, IEEE, 2016, pp. 1–2.

[19] S.T. Todd, H. Xie, An electrothermomechanical lumped element model of an electrothermal bimorph actuator, J. Microelectromech. Syst. 17 (1) (2008) 213–225.
[20] https://www.mathworks.com/products/optimization.html.

Biographies

Dingkang Wang received his B.E degree in Mechanical Engineering from Jilin University, China in 2016. He is currently working toward a Ph.D. degree in the Department of Electrical and Computer Engineering at University of Florida, Gainesville, USA. His research interests include microelectromechanical (MEMS) systems, micro/nano fabrication, and Light Detection and Ranging (LiDAR) system.

Connor Watkins received his B.S. is Electrical Engineering from the University of West Florida, Pensacola, in 2018. He is currently pursuing a Ph.D. in Electrical Engineering at the University of Florida, Gainesville. His research interests include optics, plasmonics, photonics, microelectromechanical systems (MEMS), and micro/nano fabrication

Sanjeev J. **Koppal** is an assistant professor at the University of Florida ECE department. Prior to joining UF, he was a researcher at the Texas Instruments Imaging R&D lab. Sanjeev obtained his Master's and Ph.D. degrees from the Robotics Institute at Carnegie Mellon University. After CMU, he was a postdoctoral research associate in the School of Engineering and Applied Sciences at Harvard University. He received his B.S. degree from the University of Southern California in 2003. His interests span computer vision, computational photography and optics, novel cameras and sensors, 3D reconstruction, physics-based vision and active illumination.

Huikai Xie received his B.S., M.S. and Ph.D. degrees in electrical and computer engineering from Beijing Institute of Technology, Tufts University and Carnegie Mellon University, respectively. He joined the University of Florida in 2002 as an assistant professor, where he is currently a professor at the Department of Electrical and Computer Engineering. He also worked at Tsinghua University, Robert Bosch Company, and US Air Force Research Lab. His research interests include MEMS/NEMS, integrated sensors, microactuators, integrated power passives, CNT-CMOS integration, optical MEMS, LiDAR, micro-spectrometers, optical bioimaging, and endomicroscopy. He is an associate editor of IEEE Sensors Letters, and Sensors & Actuators A. He has published over 300 technical papers and holds more than 30 patents. He is a fellow of IEEE and SPIE.